HIFiRE-5 testing in the Oxford High Density Tunnel

Samuel Broadhurst[1], Thomas Cheetham[2], Kyrolos Georgey[3], William Ivison[4],
Luke J. Doherty[5], Matthew McGilvray[6]

Abstract

This paper reports on preliminary experiments conducted in the Oxford High Density Tunnel (HDT) with a 38.1 % scale model of the HIFiRE-5 flight vehicle at Mach 7 over a range of unit Reynolds numbers between 8.5×10^6/m and 25.4×10^6/m. Model attitudes up to 2° pitch and yaw were investigated. Instrumentation and diagnostics consisted of infrared thermography, thin-film heat transfer gauges, surface pressure sensors and high-speed schlieren. The Stanton number distribution (derived from the IR measurements) was found to be comparable with previously published data from other institutions giving confidence in the diagnostics, analysis and test flow environment produced by HDT.

Keywords: *hypersonics, transition, experimental, IR, heat flux*

Nomenclature

Latin
c_p − Specific heat capacity, J/(kg K)
C, R, B, F, G − IR camera calibration constants
k − Thermal conductivity, W/(m K)
L − Length, m
M − Mach number
n − Refractive index
p − Pressure, kPa
Pr − Prandtl Number
$\dot{q}$ − Heat flux, W/m^2
Re_u − Unit Reynolds number, 1/m
Re − Reynolds number
St − Stanton number
T − Temperature, K
t − Time, s
u − Velocity, m/s
U_D − IR Camera detector signal, counts
x − Axial distance along cone, mm

Greek
α − Angle of attack, °
β − Angle of yaw, °
γ − Ratio of specific heat capacities
ϵ − Emissivity
θ − Camera view angle to pixel, °
ϕ − Azimuthal angle, °
ρ − Density, kg/m^3
τ − Transmissivity

Subscripts
0 − (Facility) Nozzle supply condition
c − Calibration
e − Boundary-layer edge condition
ne − (Facility) Nozzle exit condition
p − Pitot (pressure)
s − Shot
w − Wall condition

[1]*Research assistant, Oxford Thermofluids Institute, University of Oxford, OX2 0ES, samuel.broadhurst@some.ox.ac.uk*
[2]*Research assistant, Oxford Thermofluids Institute, University of Oxford, OX2 0ES*
[3]*Research assistant now DPhil candidate, Oxford Thermofluids Institute, University of Oxford, OX2 0ES, kyrolos.georgey@eng.ox.ac.uk*
[4]*DPhil candidate, Oxford Thermofluids Institute, University of Oxford, OX2 0ES*
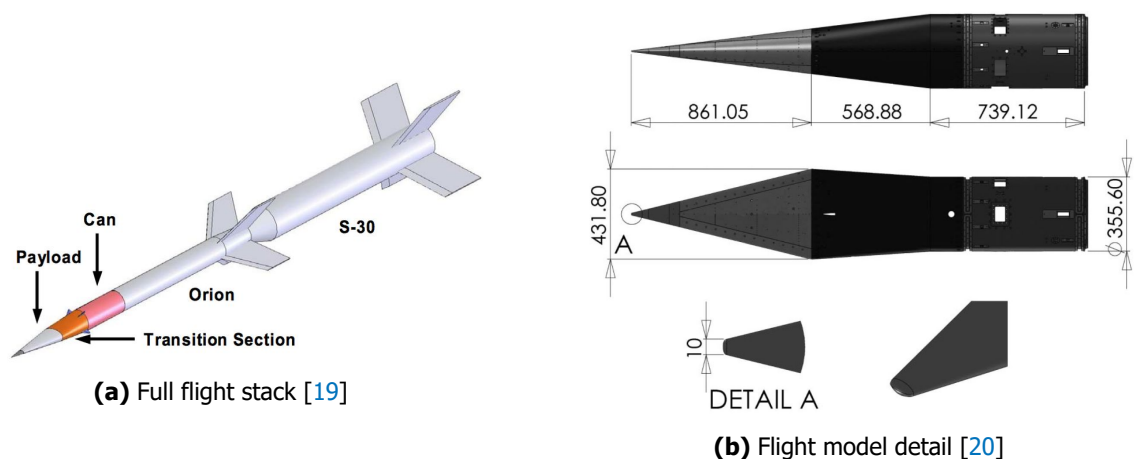[5]*Lecturer, Oxford Thermofluids Institute, University of Oxford, OX2 0ES, luke.doherty@eng.ox.ac.uk*
[6]*Professor, Oxford Thermofluids Institute, University of Oxford, OX2 0ES, matthew.mcgilvray@eng.ox.ac.uk*

1. Introduction

It is well accepted that at hypersonic velocities boundary layer transition leads to significant increases in viscous forces and heat transfer to a vehicle [1]. Despite decades of research, a general understanding of and theory for transition, irrespective of freestream velocity, is still lacking [2]. In the absence of a complete understanding, hypersonic vehicle designers must make conservative assumptions, typically resulting in lower vehicle performance or restricted flight envelopes.

Vehicle geometry, surface roughness and chemistry, the presence of steps and/or gaps, and flight condition all affect the transition process. [2, 3, 4]. As part of the Hypersonic International Flight Research Experimentation (HIFiRE) program [5, 6], two flights were specifically developed to produce high quality data sets of natural transition, enabling comparison with ground test data sets and improvement in our understanding of transition. These flights were HIFiRE-1 [3], which focussed on transition on a straight 7° half-angle cone and HIFiRE-5 [7], which investigated transition on an elliptical cone, that is 3-D geometry with partial rotational symmetry. The dominant transition mechanisms of the two flights were different, with HIFiRE-1 dominated by second Mack mode transition [3] and HIFiRE-5 dominated by cross-flow instabilities [8], and so is considered more representative of complex flight vehicles.

The flight vehicle stack for HIFiRE-5 is shown in Figure 1. It consisted of a 2:1 aspect ratio elliptical cone with half-angles of 7° (minor axis) and 13.8° (major axis). The flight article length was 0.86 m and featured a 2.5 mm nose radius. It was mated to a 2-stage booster consisting of an S-30 first stage and Improved Orion second stage booster. A second attempt was successfully flown on 18 May 2016 [9] and [10] provides a detailed report on the flight data. Specifically, the transition data on a three-dimensional geometry from the aerothermodynamic experiment was documented. Alongside the flight, scaled models of the HIFiRE-5 geometry have been tested in multiple ground test facilities around the world. References [11, 12, 13] report on experiments carried out in the Boeing/AFOSR Mach-6 Quiet Tunnel (BAM6QT) at Purdue University under both noisy and quiet flow conditions using infrared thermography (IRT). Earlier, Ref [14] reported on experiments in the same facility using temperature sensitive paint while Ref [15] conducted a study within the NASA Langley Research Center's 20-inch Mach 6 facility using phosphor thermography across a wide range of Reynolds numbers and attitudes. [16] describes tests conducted in two facilities operated by the Texas A&M National Aerothermochemistry and Hypersonic Laboratory, namely the ACE facility (noisy) and the M6QT (quiet), using IRT. Finally, Ref. [17] reports on experiments carried out in the United States Air Force Academy's (USAFA) Mach 6 Ludwieg tube. Limited IRT data was captured at Mach 7 at Calspan University of Buffalo Research Center [18].

(a) Full flight stack [19]

(b) Flight model detail [20]

Fig 1. Schematic of HIFiRE-5 flight test vehicle

This paper reports on a new 38.1 % scale model of HIFiRE-5 that has been developed at the Oxford Thermofluids Institute. The model was developed with the aim of investigating leading edge transition

in the Oxford T6 Stalker Tunnel, a multi-mode shock tunnel facility, at flight representative enthalpies. Instrumentation consists of surface pressure transducers, thin-film heat transfer gauges, alongside high-speed infrared thermography (IR) and schlieren videography. Prior to testing in T6, and to examine data self-consistency and consistency with previously published data for the HIFiRE-5 geometry, a test campaign has been conducted in the Oxford High Density Tunnel (HDT), a heated Ludwieg tube at Mach 7 and a range of attitudes. The results of these tests are reported here. Section 2 describes the experimental set up, including the HDT facility, test flow conditions, experimental model and instrumentation and the experimental data reduction. The paper continues in Section 3 with a discussion of the results, before some conclusions and an outlook to the future testing is given in Section 4.

2. Experimental Setup

2.1. Test Facility – HDT

The experiments were conducted in the University of Oxford's High-Density Tunnel (HDT) which was operated in heated Ludwieg Tube mode with a contoured Mach 7 nozzle. A schematic of the facility is provided in Figure 2. It features a steel Ludwieg tube, measuring 17.4 m in length with an internal diameter of 152.4 mm [21]. An upstream-facing, fast-acting valve separates the Ludwieg tube from a nozzle plenum volume and is used to initiate and terminate a test. The Mach 7 nozzle has an exit diameter of 351 mm and a core flow diameter of 280 mm at nozzle exit [22].
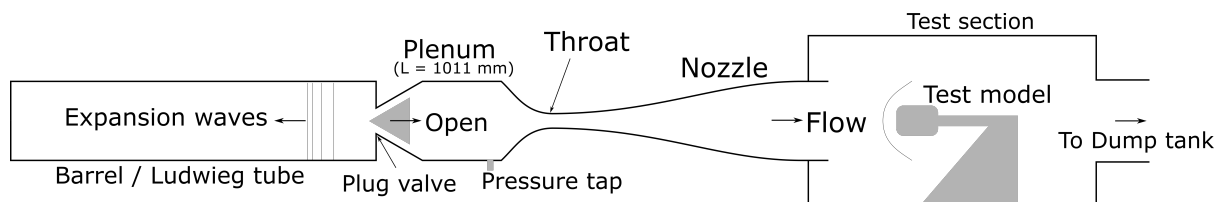

Fig 2. Schematic of the test facility [23]

2.2. Flow Conditions

The test conditions used in this work are reported in Table 1. The facility pre-heat temperature, aka fill temperature, was kept constant at 500 K producing a flow total temperature of 449 K. Nozzle supply pressures of 1446 kPa, 2040 kPa and 5110 kPa were used to provide a range of Reynolds numbers covering $t \leq 515\,\mathrm{s}$ after launch of the flight data (i.e. flight $Re_L \leq 8.6 \times 10^6$ and Mach number ≈ 7.7) [20]. The nozzle supply pressure p_0 was measured with a flush mounted Kulite XCQ-080 sensor with range 0 to 70 bar absolute. Prior to the campaign, the nozzle exit flow was characterised using a rake featuring Pitot pressure probes (instrumented with Kulites sensors) and aspirated thermocouples [24, 23] (instrumented with K-type sensors) for the measurement of total temperature. The rake data was used to generate a test flow calibration file which enables inference of the test flow conditions via. only measurement of the nozzle supply pressure. The basic assumptions of the calculation are isentropic flow to the calibrated Pitot-to-supply pressure ratio. The total-temperature is taken to be repeatable for fixed fill temperature and that the Pitot-to-supply pressure ratio is insensitive to variations in fill pressure[1]. Keyes model [25] is used for the calculation of viscosity and the test gas was pure nitrogen[2].

2.3. Model and Instrumentation

A new 38.1 % scale model of the HIFiRE-5 flight vehicle was been developed for this work. Shown in Figure 3, the model consists of six major components: a nose piece, two leading-edge pieces, upper and lower pieces and the sting-caps. The lower body piece, together with the sting-cap pieces, integrate with a "standardised" model mounting sting used by the Oxford Hypersonics Group. This sting allows mounting to a two-axis traverse mechanism providing ±15° movement in pitch and ±5° in yaw/side-slip. Ref [22] previously demonstrated model alignment to within 0.1° in both pitch and yaw using this traverse with appropriately located sensors on a model. Figure 4 provide a photograph, as viewed from

---

[1]Nozzle survey results that are in preparation for publication confirm this assumption.
[2]Specifically, oxygen-free nitrogen supplied by BOC Ltd.

Table 1. Test Flow Conditions

| Quantity | Unit | Condition | | |
		1 'Low' Re_u	**2** 'Medium' Re_u	**3** 'High' Re_u
p_0	kPa	1446 ± 7	2040 ± 7	4338 ± 7
T_0	K	449 ± 15	449 ± 15	449 ± 15
p_p	kPa	20.5 ± 0.5	28.9 ± 0.5	61.4 ± 0.5
M_{ne}		7.13 ± 0.04	7.13 ± 0.03	7.13 ± 0.01
u_{ne}	m/s	922 ± 15	922 ± 15	922 ± 15
p_{ne}	Pa	310 ± 11	438 ± 11	932 ± 11
T_{ne}	K	40.2 ± 1.4	40.2 ± 1.4	40.2 ± 1.3
$Re_{u,ne}$	10^6/m	8.5 ± 0.4	11.9 ± 0.6	25.4 ± 1.3
Re_L	10^6/m	2.78 ± 0.13	3.90 ± 0.20	8.32 ± 0.43

the IR camera side of the test section, of the model installed in the HDT test section with the Mach 7 facility nozzle.

Overall the model is 350 mm in length from a virtual sharp nose tip, 15 mm longer than the model of Ref. [12]. Several nose pieces were machined from UNS S32205 F60 stainless steel with a range of nose bluntness radii, thereby providing flexibility to destabilize the boundary on the model if desired. In the experiments reported here, the nose bluntness in the minor axis symmetry plane was 0.96 mm (consistent with design scale of the model).

The upper body component was machined from Victrex 450G Natural Polyether Ether Ketone (PEEK) to enable infrared thermography (IRT). The primary instrumentation of the upper body consists of six Kulite XCS-062 absolute pressures sensors with range 10 psi. The locations of these sensors were chosen to be consistent with locations 2, 8, 14, 19, 20 and 21 reported in [12], thereby enabling cross-facility comparisons. These sensors are denoted K2, K8, K14 etc.

Supplementary instrumentation on the upper body component included three Kulite XCQ-080 absolute pressure sensors with range 1.7 bar, labelled AoY1, AoY2 and AoA1, and two thin-film heat transfer sensors. These Kulites are used in combination with a corresponding sensor on the lower body component (labelled AoA2) for the alignment of the model with the nozzle exit flow. The thin-film heat transfer sensors, labelled HTG2 and HTG3, enable comparison with the IRT measurement. All supplementary sensors were positioned downstream of the primary instrumentation to reduce unwanted interactions. The lower body component forms the main structure of the model. It was machined from billet 7075-T6 aluminium and instrumented with four PCB132B38 pressure sensors and a single Kulite XCQ-080 absolute pressure sensor with range 1.7 bar. This Kulite (AoA2) was positioned on the minor axis symmetry line, directly opposite sensor AoA1 in the upper body component. The PCB sensors similarly match locations 2, 8, 14 and 19 reported in [12]. These were included to provide higher frequency pressure fluctuation content in later planned tests in the T6 Stalker Tunnel.

The two detachable leading-edges were developed to offer flexibility with instrumentation. In the current work, one leading edge was aluminium while the other was machined from PEEK, for IRT measurements. The PEEK leading edge was additionally instrumented with a single thin-film heat transfer gauge, labelled HTG1.

The IR camera used in the experiments was a Telops FAST Mk3 mid-wave infrared camera. It was fitted with a 50 mm lens and was set to record at 4 kfps at a resolution of 320 x 128 pixels, with an exposure
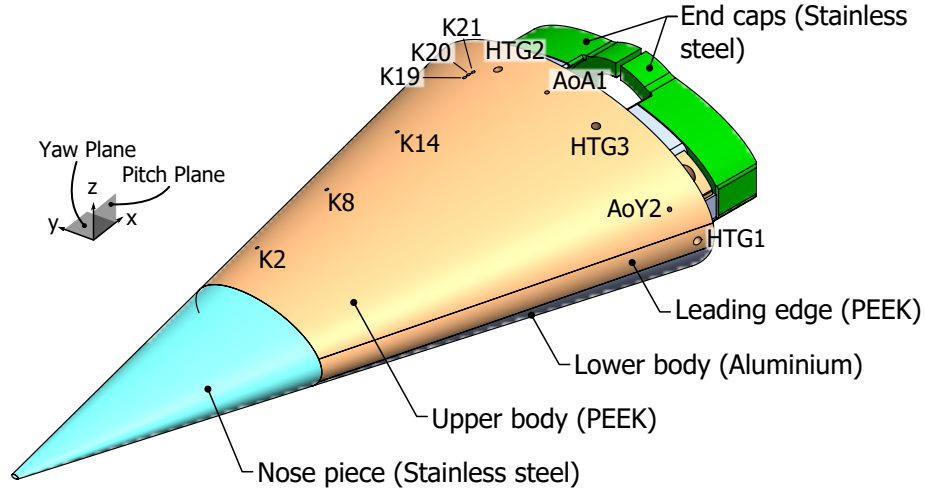
Fig 3. Oxford HIFiRE-5 model, including sensor labels. Note that sensors AoA2, AoY1 and PCB2, PCB8, PCB14 and PCB19 are not visible.
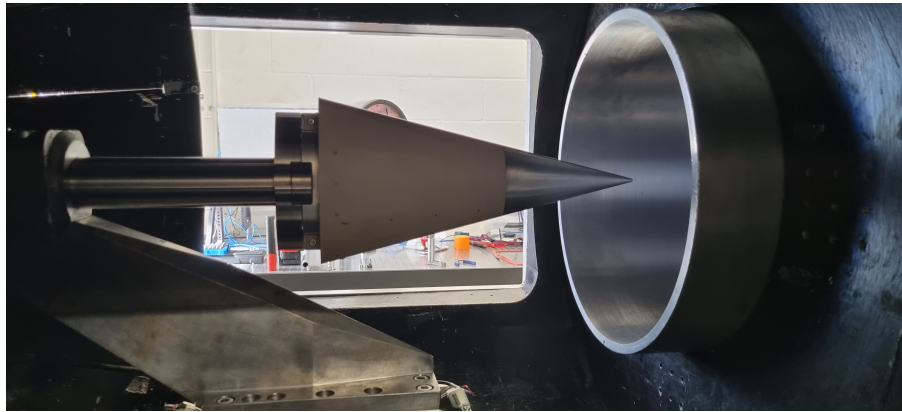
Fig 4. Oxford HIFiRE-5 model installed in the HDT test section as viewed from the IR camera side. Flow is from right to left.

time of 90 μs. The field of view encompassed the entirety of the model (in planform orientation) with a spatial scaling of approximately 1.22 mm/pixel. There was some variation in spatial scaling due to model shape and perspective changes. The camera was located approximately 500 mm from the facility centreline and viewed the model through a 5 mm thick sapphire window.

2.4. Data Reduction

IRT data are presented in Section 3 in the form of Stanton number, thereby enabling comparison with prior published results. The Stanton number was calculated using –

$$St = \frac{\dot{q}}{\rho_{ne} u_{ne} c_p \left(T_0 - T_w\right)} \qquad (1)$$

where ρ_{ne}, u_{ne} are the calculated test flow density and velocity (respectively), $c_p = 1039 \, \text{J}/(\text{kg K})$ is the specific heat of nitrogen, T_0 is the nozzle supply temperature (i.e. flow total temperature), T_w is the model wall temperature and $\dot{q}$ is the wall heat flux, both of which are calculated from the IR camera data for each pixel.

The IR camera data was converted from measured counts on each pixel to model surface temperature

using the methodology outlined in [26] based on the work of [27, 28]. A brief summary is provided here for completeness.

The in-band radiance measured by the camera during a test is given by –

$$U_D = \frac{CR}{e^{B/T_w} - F} + G_s \tag{2}$$

where U_D is the number of counts recorded by the camera detector; R, B, and F are constants specific to the set up (camera and optical elements) and are determined via in-situ calibration; C is a constant that accounts for differences in the emissivity and transmissivity between the test and calibration; G is a constant that accounts for radiation reflected from the model and being emitted from objects in the optical path; and T_w is the model surface temperature (of interest).

Constant G is different between the shot and calibration but can be determined from data recorded prior to flow arrival subject to the assumptions it remains constant during the shot and the pre-shot temperature of the model is equal to ambient [26]. Constant C is given by –

$$C = \frac{\epsilon_s \tau_s}{\epsilon_c \tau_c} \tag{3}$$

where subscript s refers to the shot, subscript c refers to the in-situ calibration, $\epsilon(\theta)$ is the emissivity of the material imaged by the camera and is a function of viewing angle θ, and τ is the transmissivity of the gas between the surface of interest and camera. The difference in transmissivity is a consequence of the calibration being performed under atmospheric conditions while the test gas was nitrogen. A value $\tau_s/\tau_c = 0.9764$ was used based on transmissivity data from [29]. The manufacture quoted value for the calibrator emissivity was used for ϵ_c (given below) and, due to the significant curvature in the model surface near the leadings edges, the emissivity during the shot (ϵ_s) was calculated using the following equation [30] –

$$\epsilon(\theta) = \frac{2\cos(\theta) \cdot \sqrt{n^2 - \sin^2(\theta)}}{\left(\cos(\theta) + \sqrt{n^2 - \sin^2(\theta)}\right)^2} \cdot \left(1 + \frac{n^2}{\left(\cos(\theta) \cdot \sqrt{n^2 - \sin^2(\theta)} + \sin^2(\theta)\right)^2}\right) \tag{4}$$

where θ is the viewing angle and n is the refractive index and was taken to be 1.8 ± 0.1 for PEEK. The camera position relative to the model was calculated from known locations of specific pixels, which, in combination with the CAD geometry, gave the angle between camera axis and the model surface normal vector for each pixel.

A CI-Systems SR-33N-7A extended area blackbody calibrator was used for the in-situ calibration of the camera set up. It features a flat calibration surface that 178 mm square in size, has a quoted emissivity of 0.98, spatial uniformity of 0.01 K and temperature accuracy of 0.05 K. This calibrator was positioned in the test section in place of the model. Due to the overall field of view, two sets of calibration data were recorded, one with the calibrator located upstream and one with the calibrator located downstream. Due to slight mistake in positioning of the calibrator, there was insufficient spatial overlap of the two sets of calibration data, resulting in a narrow band of approximately 10 pixels for which no usable calibration data was recorded. This band of pixels was excluded from further analysis.

Calibration temperatures over the range 10 to 45 °C were recorded with consistent camera framerate, lens, position and exposure time as used in the actual tests. The discrete calibration data points were interpolated using a shape-preserving piece-wise cubic method, thereby providing a calibration curve relating raw counts to calibrator temperature for each camera pixel.

Each IR camera pixel was treated as a discrete temperature sensor and converted to surface heat flux using the impulse response convolution approach of Ref. [31]. This method relates the surface temperature response to heat flux by assuming a 1D semi-infinite solution to the heat equation –

$$T(t) = \frac{2}{\sqrt{\pi}} \frac{\dot{q}}{\sqrt{\rho c_p k}} t^{0.5} \tag{5}$$

The thermal product of PEEK over a temperature range 25 °C to 80 °C was taken to be $\sqrt{\rho c_p k} = (642 \pm 56)\,\mathrm{J/m^2/K^2/\sqrt{s}}$. This value is based on experimental measurement of the thermal diffusivity, specific heat capacity and room temperature bulk density conducted by NETZSCH Application Laboratory for a sample taken from the same manufacturing batch of PEEK that the model components were machined from. The uncertainty represents two standard deviation variation over the temperature range. The calculated transient heat flux was averaged over the steady test period prior to substitution into Equation (1).

3. Results

Heat flux data calculated from the IR camera data are presented in this section in the form of Stanton number. Section 3.1 discusses results across a range of Reynolds numbers where the model is aligned with the nozzle exit flow (i.e. 0° pitch and yaw). Sections 3.2 and 3.3 presents results at a single Reynolds number when the model is pitched and yawed, respectively. Finally, Section 3.4 presents a qualitative comparison of the current HDT results to prior data from a range of low enthalpy facilities. Note that images from the current work have been mirrored (flipped) about a vertical plane such that flow is from left-to-right (by convention, cf. Figure 4).

3.1. 0° Pitch and Yaw

Figure 5 presents Stanton number distributions for each test condition (Table 1) used in this work. Regions of higher Stanton number represent regions of transitioned flow. Examining the results, the expected influence of Reynolds number is captured – that is, the transition front moves upstream and outward from the centreline with increasing Reynolds numbers. At all three conditions axial streaks of lower the heat transfer are visible both along the centreline and either side of centreline are clearly resolved. These are a consequence of boundary layer roll-up and 'mush-rooming' induced by the geometry and has been previously observed (see Section 3.4 and well discussed in the literature. The spatial distributions of conditions 1 and 2 are quite similar, with the most noticeable different being the upstream shift of the transition front (streaks) either side of the centreline. This is not unexpected given the relative similarity on Reynolds number (condition 2 is 40 % higher than condition 1). Condition 3 is more than double the Reynolds number of condition 2 and produces a significant change in the heat transfer distribution. The transition front is now almost coincident with the leading edges and extends upstream of the measurement surface. Similar results have previously been reported, as discussed in Section 3.4.

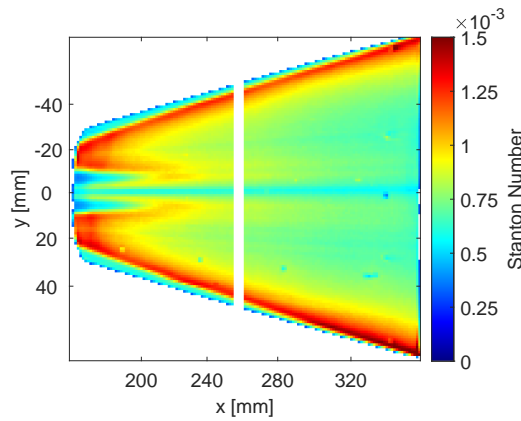### 3.2. Influence of pitch angle

The effect of pitch angle on heat transfer distribution and transition on HiFIRE-5 has been investigated previously [12]. Figure 6 presents results from the current work for both a flow aligned test ($\alpha = 0°$) and a test where the model was pitched at 2° such that the IR camera was viewing the leeward side. Both tests were conducted at condition 2. The result is as expected with the Stanton number of the pitched model overall lower than the model at 0° pitch. The streaks of low heat transfer (laminar flow) at $y = \pm 10\,\mathrm{mm}$ in Figure 6a have become narrower and shifted towards the centreline in Figure 6b resulting in an upstream shift of the transition front. This may be attributed to the lower pressure (on the leeward face) producing less boundary layer roll up on the model centreline compared with the 0° pitch case. Examining Stanton number distribution Figure 6b closely, some slight asymmetry between the upper and lower halves of the figure is apparent. Specifically the shape of the transition front at $(x, y) = (160, \pm 10)\,\mathrm{mm}$ and higher heat transfer at $(x, y) = (280, 40)\,\mathrm{mm}$ and $(x, y) = (360, 60)\,\mathrm{mm}$. The cause of these differences is not clear as they do not seem related to the instrumentation holes. Further investigation of the tested geometry is required to determine any issues at the interface of the separate leading edge piece and upper body (Figure 3).

3.3. Influence of yaw angle

Figure 7 presents results from the current work for both a flow aligned test ($\beta = 0°$) and a test where the model was yawed at $-2°$. Both tests were conducted at condition 2. The results confirm what is known from the literature – that this geometry is sensitive to yaw. That is, the change in heat transfer distribution is more pronounced for yaw than for pitch. In Figure 7b, the heat transfer distribution features many of the same patterns as the non-yawed distribution (Figure 7a) but is modified to follow
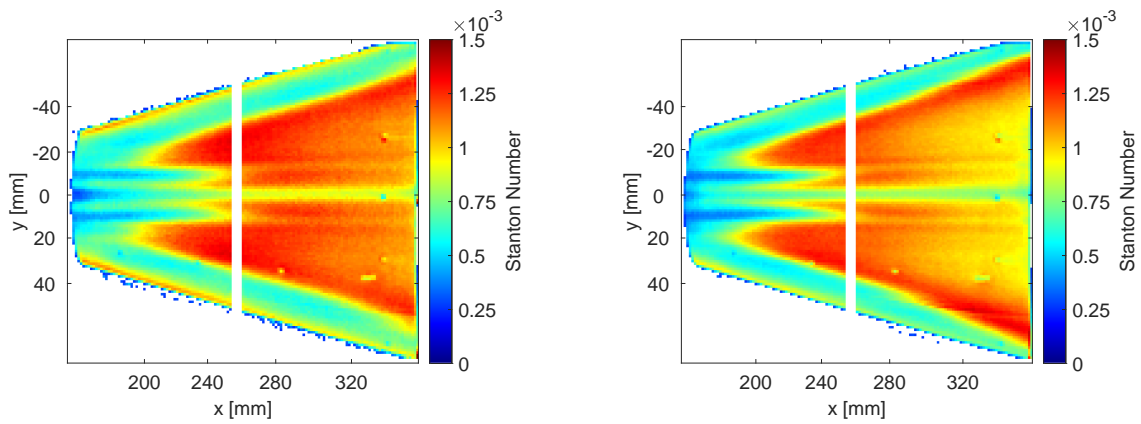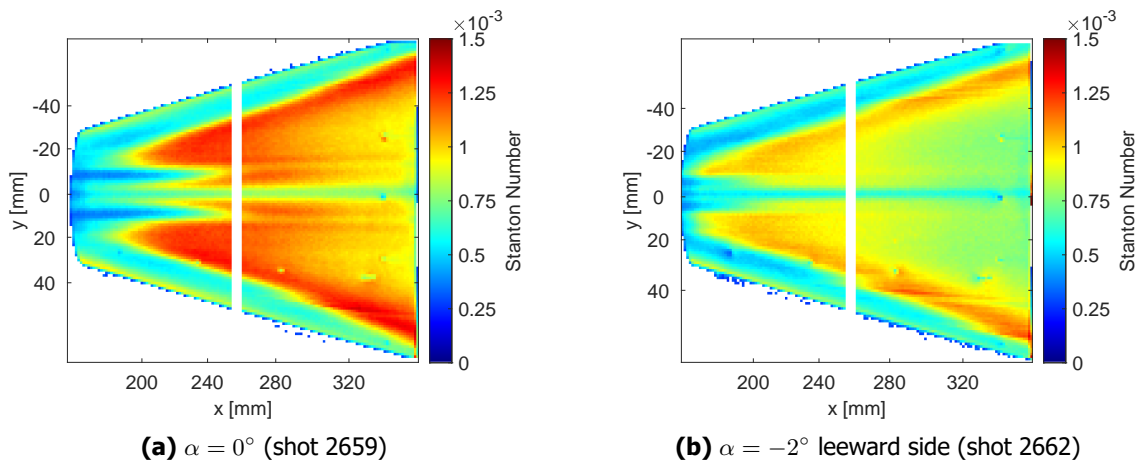
(a) Condition 1, $Re_u = (8.5 \pm 0.4) \times 10^6/\text{m}$ (shot 2655)   **(b)** Condition 2, $Re_u = (11.9 \pm 0.6) \times 10^6/\text{m}$ (shot 2659)


(c) Condition 3, $Re_u = (25.4 \pm 1.3) \times 10^6/\text{m}$ (shot 2657)

Fig 5. Stanton number distribution for $\alpha = \beta = 0°$ across a range of unit Reynolds numbers.

(a) $\alpha = 0°$ (shot 2659)   **(b)** $\alpha = -2°$ leeward side (shot 2662)

**Fig 6.** Influence of pitch angle on Stanton number distribution for condition 2, $Re_u = (11.9 \pm 0.6) \times 10^6/\text{m}$

the streamlines. As a consequence, the transition front for $y > -10\,\mathrm{mm}$ and the region of laminar flow that is typically down the middle are both angled across the model. The transition front on the windward side of the model is shifted slightly further away from the leading edge than for the non-yawed case but extends further upstream near the model centreline. Finally, there is a region of higher heat transfer (than the non-yawed results) at $(x, y) = (> 280, < -30)\mathrm{mm}$.

(a) $\alpha = 0°$ (shot 2659) **(b)** $\beta = -2°$ (shot 2660)
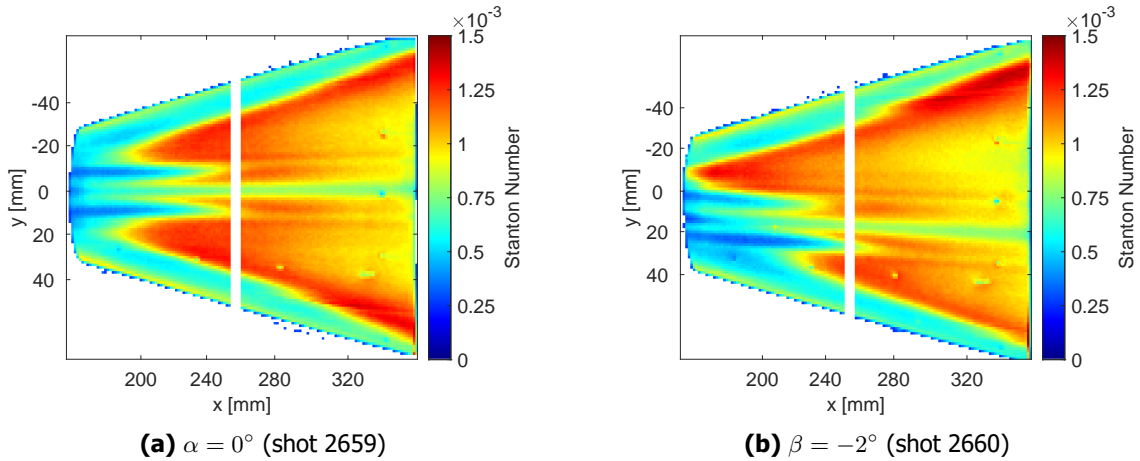
Fig 7. Influence of yaw angle on Stanton number distribution for condition 2, $Re_u = (11.9 \pm 0.6) \times 10^6/\mathrm{m}$.

3.4. Qualitative comparison to previous ground testing

Ground testing of the 38.1 % subscale HIFiRE-5 model has previously been undertaken in several hypersonic tunnels located in the USA. To compare the data from the Oxford HDT testing, cases where similar total enthalpy, Reynolds numbers and noise level were extracted from the literature from the Purdue BAM6QT (run noisy) [14], NASA LaRC 20" tunnel [15], Texas A&M ACE tunnel [16] and USAFA Ludwieg tunnel [17]. Each of these historical tests have several differences to the current Oxford HDT tests as detailed below:

1. The exact Reynolds number was not matched in all tests. Consequently, the closest possible case was chosen for each and it is therefore expected the transition location will shift accordingly.

2. The tests were at a lower Mach number of approximately 6 instead of the Mach 7 as for the Oxford tests. A change of this magnitude has been found in previous experimental testing on cones at angle of attack to make only a minimal difference in the heat flux distribution.

3. The surface temperature distribution varies between short duration testing (approximately room temperature ≈290 K) and longer duration testing (≈313 K for the BAM6QT tests). This will have a minor effect on the transition process.

4. Each tunnel has different freestream noise levels. This will mean that transition location will likely change, altering the comparable Reynolds number. In particular, the USAFA Ludwieg tunnel data has high freestream noise level due to the downstream facing plug valve that seals on the nozzle throat.

These factors make direct quantitative comparison meaningless, however, qualitative comparison of the heat flux distribution and Stanton number levels can be used to ensure the current model and associated measurement techniques are satisfactorily commissioned.

To undertake qualitative comparisons, data was extracted from the relevant papers and converted, where sufficient information was provided, into non-dimensional heat transfer (i.e. Stanton number). Four comparisons are provided in Figures 8 to 11. Figure 8 presents a comparison of the heating distribution for the low Reynolds number condition (condition 1). All five tests have unit Reynolds numbers in the range $6 \times 10^6/\mathrm{m}$ to $10.1 \times 10^6/\mathrm{m}$ and are seen to have comparable heating distributions, with the edges
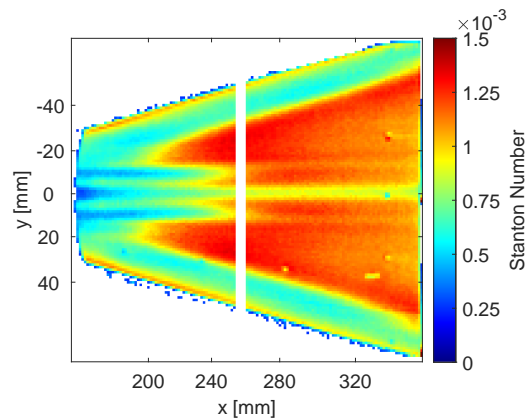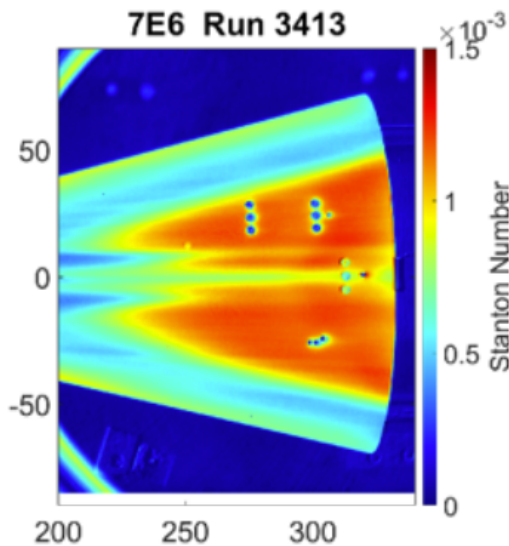
(a) Oxford HDT, Mach 7, $Re_u = 8.5 \times 10^6/\text{m}$ (shot 2655)
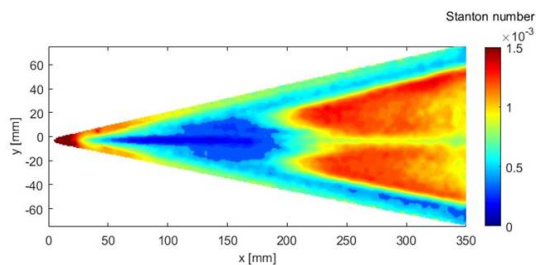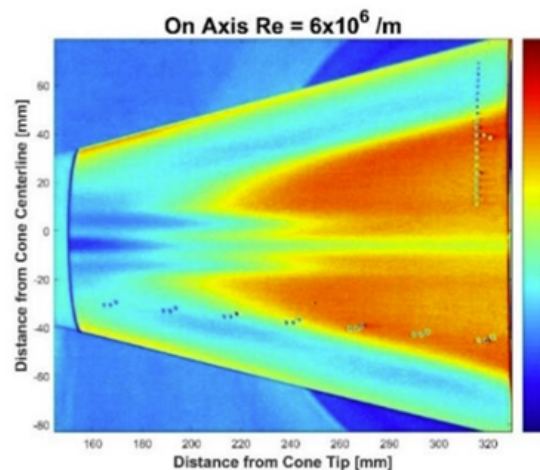

(b) NASA LaRC 20", Mach 6, $Re_u = 10.1 \times 10^6/\text{m}$ [15, Figure 5 adapted to Stanton number]
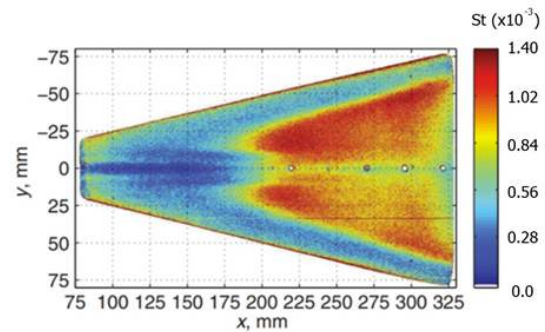
(c) BAM6QT (noisy), Mach 6, $Re_u = 8.1 \times 10^6/\text{m}$ [14, Figure 18(c) adapted to Stanton number]

(d) Texas A&M ACE, Mach 6, $Re_u = 7 \times 10^6/\text{m}$ [16, Figure 21]
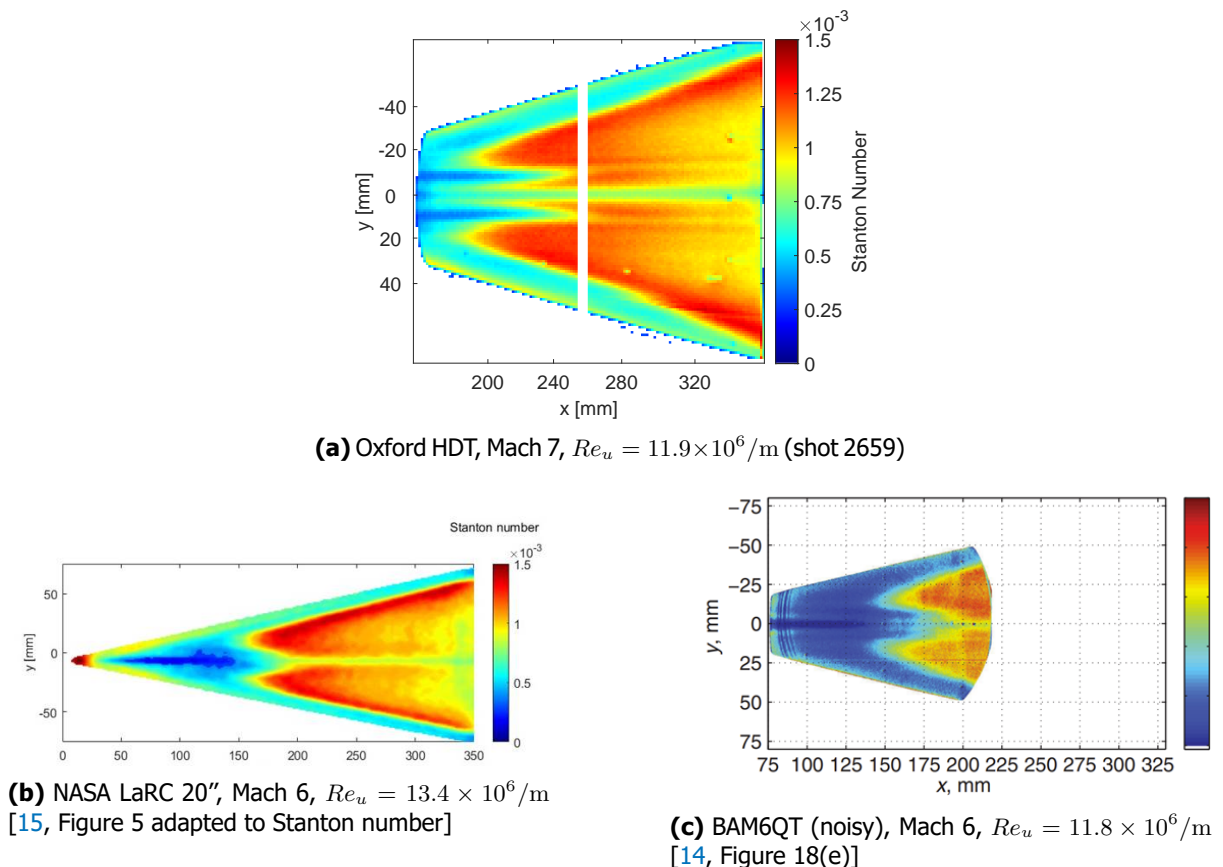

(e) USAFA Ludwieg Tunnel (on-axis), Mach 6, $Re_u = 6 \times 10^6/\text{m}$ [17, Figure 11]

Fig 8. Qualitative comparison of Stanton number distribution from different low total enthalpy ground tests at condition 1 at $\alpha = \beta = 0°$. Note: The original USAFA data was in heat flux, but no information on surface temperature and freestream was provided to enable conversion to Stanton number.

showing higher heating, symmetric high heating lobes slightly off-axis and a low heating area on the axis. Overall, the current results better resolve features in the distribution than the NASA LaRC and Purdue BAM6QT results, which used phosphor thermography and temperature sensitive paint respectively and has a more symmetric distribution than the Texas A&M ACE results. The Stanton number magnitudes are very similar in all four cases where a comparison is possible. A similar conclusion can also be drawn for the mid Reynolds number condition (condition 2) as seen in Figure 9, where both the Stanton number magnitude and distribution from the current work is similar to the NASA LaRC and Purdue data, where the transition front has progressed forward on the cone.

For the high Reynolds number condition (condition 3), Figure 10, the transition has progressed upstream of the field of view in the current data but can be clearly seen in the NASA LaRC data. Again, the data's Stanton number distribution and magnitude are very close to each other. Despite the limited spatial extent of the current work compared with the NASA LaRC data, the spatial resolution (of features) is better, thus demonstrating the improved capability of current IR cameras compared with other techniques, as has been previously found by other researchers [13].

Finally, a comparison of the heating when at a pitch angle of $-2°$ (leeward side) can also be made to the NASA LaRC data. This is given in Figure 11 and shows a supressed heating and a similar transition front to each other. It can be concluded from these comparisons, that the model and processing methods are satisfactorily qualified for future testing.

(a) Oxford HDT, Mach 7, $Re_u = 11.9 \times 10^6/\text{m}$ (shot 2659)

(b) NASA LaRC 20", Mach 6, $Re_u = 13.4 \times 10^6/\text{m}$ [15, Figure 5 adapted to Stanton number]

(c) BAM6QT (noisy), Mach 6, $Re_u = 11.8 \times 10^6/\text{m}$ [14, Figure 18(e)]

Fig 9. Qualitative comparison of Stanton number distribution from different low total enthalpy ground tests at condition 2 at $\alpha = \beta = 0°$. Note: The original BAM6QT data for this case was in heat flux, but no information on surface temperature was provided to enable conversion to Stanton number.
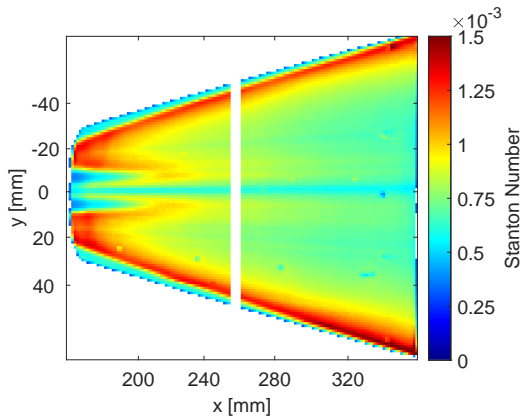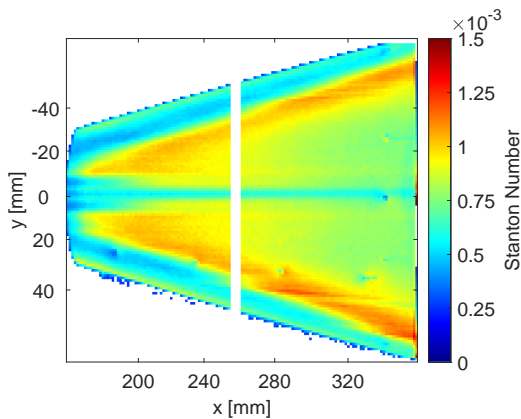
(a) Oxford HDT, Mach 7, $Re_u = 25.4 \times 10^6/\text{m}$ (shot 2657)
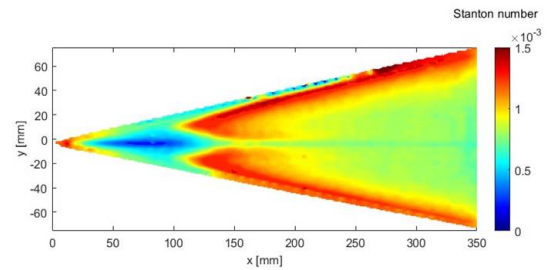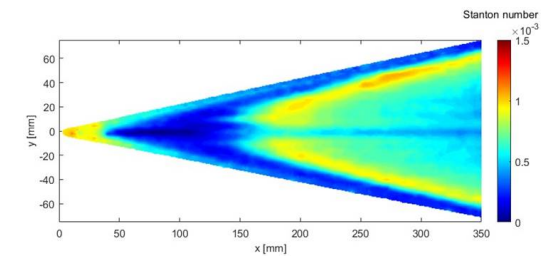

(b) NASA LaRC 20", Mach 6, $Re_u = 23 \times 10^6/\text{m}$ [15, Figure 5 adapted to Stanton number]

Fig 10. Qualitative comparison of Stanton number distribution from different low total enthalpy ground tests at condition 3 at $\alpha = \beta = 0°$

(a) Oxford HDT, Mach 7, $Re_u = 11.9 \times 10^6/\text{m}$ (shot 2662)

(b) NASA LaRC 20", Mach 6, $Re_u = 13.4 \times 10^6/\text{m}$ [15, Figure 8 adapted to Stanton number]

Fig 11. Qualitative comparison of heating from different low total enthalpy ground tests at condition 2 at $\alpha = -2°$

4. Conclusion

A 38.1 % scale HIFiRE-5 model has been constructed, instrumented, and tested to characterize the flow around its 3-D geometry. The new test article underwent testing in the Oxford High Density Tunnel. Analysis of the data collected during this testing campaign has demonstrated self-consistency across various instrumentation techniques. This consistency provides confidence in the functionality of the instrumentation on the model and the data processing methodologies employed. Furthermore, the collected data aligns with findings from previous ground testing conducted on other HIFiRE-5 models. Specifically, infrared imaging revealed corresponding streaks of high and low heat flux, indicative of turbulent and laminar flows, respectively. Moreover, the observed effects of pitch and yaw corroborate patterns outlined in prior studies. This consistency with previous research suggests the absence of any issues with the test article, instrumentation, or experimental setup, alleviating concerns in this regard. The Oxford model is, therefore, deemed ready for testing under higher enthalpy conditions in the University of Oxford's T6 Stalker Tunnel.

Acknowledgements

References

[1] van Driest, E.R.: The Problem of Aerodynamic Heating. Aeronautical Engineering Review, 15:26–41 (1956)

[2] Schneider, S.P.: Effects of Roughness on Hypersonic Boundary-Layer Transition. Journal of Spacecraft and Rockets, 45(2):193–209 (2008). URL `http://dx.doi.org/10.2514/1.29713`

[3] Kimmel, R.L., Adamczak, D., Gaitonde, D., Rougeux, A., Hayes, J.: HIFiRE-1 Boundary Layer Transition Experiment Design. 45th AIAA Aserospace Sciences Meeting and Exhibit. AIAA-2007-534, Reno, Nevada, USA (2007). URL `http://dx.doi.org/10.2514/6.2007-534`

[4] Johnson, H.B., Seipp, T.G., Candler, G.V.: Numerical Study of a Hypersonic Reacting Boundary Layer Transition on Cones. Physics of Fluids, 10(10) (1998). URL `http://dx.doi.org/10.1063/1.869781`

[5] Dolvin, D.J.: Hypersonic International Flight Research and Experimentation (HIFiRE) Fundamental Science and Technology Development Strategy. 15th AIAA International Space Planes and Hypersonic Systems and Technologies Conference. AIAA-2008-2581, Dayton, Ohio, USA (2008). URL `http://dx.doi.org/10.2514/6.2008-2581`

[6] Dolvin, D.J.: Hypersonic International Flight Research and Experimentation Technology Development and Flight Certification Strategy. 16th AIAA/DLR/DGLR International Space Planes and Hypersonic Systems and Technologies Conference. AIAA-2009-7228, Bremen, Germany (2009). URL `http://dx.doi.org/10.2514/6.2009-7228`

[7] Juliano, T.J., Adamczak, D., Kimmel, R.L.: HIFiRE-5 Flight Test Results. Journal of Spacecraft and Rockets, 52(3):650–663 (2015). URL `http://dx.doi.org/10.2514/1.A33142`

[8] Kimmel, R., Adamczak, D., Juliano, T.J.: HIFiRE-5 Flight Test Preliminary Results. 51st AIAA Aerospace Sciences Meeting. AIAA-2013-377, Dallas, Texas, USA (2013). URL `http://dx.doi.org/10.2514/6.2013-377`

[9] Kimmel, R.L., Adamczak, D.W., Hartley, D., Alesi, H., Frost, M.A., Pietsch, R., Shannon, J., Silvester, T.: Hypersonic International Flight Research and Experimentation-5b Flight Overview. Journal of Spacecraft and Rockets, 55(6) (2018). URL `http://dx.doi.org/10.2514/1.A34148`

[10] Juliano, T., Poggie, J., Porter, K., Kimmel, R., Jewell, J., Adamczak, D.: HIFIRE-5b Heat Flux and Boundary-Layer Transition. Journal of Spacecraft and Rockets, 55:1–14 (2018). URL `http://dx.doi.org/10.2514/1.A34147`

[11] Borg, M.P., Kimmel, R.L., Stanfield, S.: Traveling Crossflow Instability for the HIFiRE-5 Elliptic Cone. Journal of Spacecraft and Rockets, 52(3):664–673 (2015). URL `http://dx.doi.org/10.2514/1.A33145`

[12] Borg, M.P., Kimmel, R.L.: Ground Test of Transition for HIFiRE-5b at Flight-Relevant Attitudes. Journal of Spacecraft and Rockets, 55(6):1329–1340 (2018). URL `http://dx.doi.org/10.2514/1.A34163`

[13] Juliano, T.J., Paquin, L.A., Borg, M.P.: HIFiRE-5 Boundary-Layer Transition Measured in a Mach-6 Quiet Tunnel with Infrared Thermography. AIAA Journal, 57(5):2001–2010 (2019). URL http://dx.doi.org/10.2514/1.J056750

[14] Juliano, T.J., Borg, M.P., Schneider, S.P.: Quiet Tunnel Measurements of HIFiRE-5 Boundary-Layer Transition. AIAA Journal, 53(4):832–846 (2015). URL http://dx.doi.org/10.2514/1.J053189

[15] Berger, K.T., Rufer, S.J., Kimmel, R., Adamczak, D.: Aerothermodynamic Characteristics of Boundary Layer Transition and Trip Effectiveness of the HIFiRE Flight 5 Vehicle. 39th AIAA Fluid Dynamics Conference. AIAA-2009-4055, San Antonio, Texas, USA (2009). URL http://dx.doi.org/10.2514/6.2009-4055

[16] Neel, I.T., Leidy, A.N., Tichenor, N.R., Bowersox, R.D.W.: Characterization of Environmental Disturbances on Hypersonic Crossflow Instability on the HIFiRE-5 Elliptic Cone. AIAA SPACE Forum. AIAA-2018-5375, Orlando, Florida, USA (2018). URL http://dx.doi.org/10.2514/6.2018-5375

[17] Hembling, E., Wirth, J., Semper, M.: Hypersonic Crossflow Investigation on the HIFIRE-5 Elliptic Cone. AIAA SciTech Forum. AIAA-2021-0005, Virtual Event (2021). URL http://dx.doi.org/10.2514/6.2021-0005

[18] Kimmel, R.L., Adamczak, D., Borg, M.P., Jewell, J.S., Juliano, T.J., Stanfield, S., Berger, K.: HIFiRE-1 and -5 Flight and Ground Tests. 2018 AIAA Aerospace Sciences Meeting. AIAA, Kissimmee, Florida, USA (2018). URL http://dx.doi.org/10.2514/6.2018-0056

[19] Kimmel, R.L., Adamczak, D., Berger, K., Choudhari, M.: HIFiRE-5 Flight Vehicle Design. 40th Fluid Dynamics Conference and Exhibit. AIAA-2010-4985, Chicago, Illinois, USA (2010). URL http://dx.doi.org/10.2514/6.2010-4985

[20] Juliano, T.J., Jewell, J.S., Kimmel, R.L.: HIFiRE-5b Boundary-Layer Transition Length and Turbulent Overshoot. Journal of Spacecraft and Rockets, 58(2):265–283 (2021). URL http://dx.doi.org/10.2514/1.A34856

[21] McGilvray, M., Doherty, L.J., Neely, A.J., Ireland, P.T., Pearce, R.: The Oxford High Density Tunnel. 20th AIAA International Space Planes and Hypersonic Systems and Technologies Conference. AIAA-2015-3548, Glasgow, Scotland (2015). URL http://dx.doi.org/10.2514/6.2015-3548

[22] Wylie, S., Doherty, L.J., McGilvray, M.: Commissioning of the Oxford High Density Tunnel for Boundary Layer Stability Measurements at Mach 7. 48th AIAA Fluid Dynamics Conference. AIAA 2018-3074 (2018). URL http://dx.doi.org/10.2514/6.2018-3074

[23] Hermann, T., McGilvray, M., Hambidge, C., Doherty, L.J., Buttsworth, D.: Total Temperature Measurements in the Oxford High Density Tunnel. International Conference on Flight Vehicles Aerothermodynamics and Re-entry Mission & Engineering (FAR). ESA, Monopoli, Italy (2019)

[24] Widodo, A., Buttsworth, D.: Stagnation Temperature in a Cold Hypersonic Flow Produced by a Light Free Piston Compression Facility. Experiments in Fluids, 54(1486) (2013). URL http://dx.doi.org/10.1007/s00348-013-1486-6

[25] Keyes, F.G.: A summary of viscosity and heat-conduction data for He, Ar, H2, O2, N2, CO, CO2, H2O, and Air. Transactions of the American Society of Mechanical Engineers, 73(5):589–595 (1951)

[26] Ivison, W., Hambidge, C.J., McGilvray, M., Flinton, A., Merrifield, J., Steelant, J.: Heat Flux Augmentation Caused by Surface Imperfections in Turbulent Boundary Layers. HiSST: 3rd International Conference on High-Speed Vehicle Science & Technology. Council of European Aerospace Societies, Busan, Korea (2024)

[27] Astarita, T, Carlomagno, M.: Infrared Thermography for Thermo-Fluid-Dynamics. Experimental Fluid Mechnaics. Springer Berlin, Heidelberg, first ed. (2012). URL http://dx.doi.org/10.1007/978-3-642-29508-9

[28] Zaccara, M., Edelman, J.B., Cardone, G.: A General Procedure for Infrared Thermography Heat Transfer Measurements in Hypersonic Wind Tunnels. International Journal of Heat and Mass Transfer, 163(120419) (2020). URL http://dx.doi.org/10.1016/j.ijheatmasstransfer.2020.120419

[29] Mikhailenko, S.N., Babikov, Y.L., Golovko, V.F.: Information-calculating system Spectroscopy of Atmpsoheric Gases: the structure and main functions. Atmospheric and oceanic optics, 18(9):685–695 (2005). URL https://ao.iao.ru/en/content/vol.18-2005/iss.09/4

[30] Baehr, H.D., Stephan, K.: Heat and Mass Transfer. Springer, Berlin, Heidelberg (2006)

[31] Oldfield, M.L.G.: Impulse Response Processing of Transient Heat Transfer Gauge Signals. Journal of Turbomachinery, 130(2):021023 (2008). URL http://dx.doi.org/10.1115/1.2752188